

# Tracking the baryon number with nuclear collisions

Short Title: Do quarks or gluons carry baryon number?

The STAR Collaboration

**Baryon quantum number is believed to be conserved since baryogenesis in the early Universe. While fractionally charged valence quarks are understood conventionally to each carry a baryon number of  $1/3$ , the baryon junction, a non-perturbative Y-shaped topology of neutral gluons, has also been proposed as an alternative entity tracing the baryon number. Neither scenario has been verified experimentally. The STAR Collaboration reports measurements at mid-rapidity of baryon number ( $B$ ) over the electric charge number difference ( $\Delta Q$ ) in isobar nuclear collisions, and the net-proton yield along rapidity in photonuclear collisions. A larger  $B/\Delta Q$  ratio and less asymmetric net-proton yield are observed than predicted from models assigning baryon number to valence quarks. These findings, corroborated by previous measurements in Au+Au collisions, disfavor the valence quark picture.**

There are a few fundamental conservation laws in physics that govern the evolution of the existing world. Among them, baryon number ( $B$ ) is believed to have been conserved since baryogenesis shortly after the birth of the Universe (1, 2). It is a quantity that is associated with hadrons containing three quarks, such as protons and neutrons, and dictates the baryon asymmetry in the present Universe. The Standard Model provides a framework for understanding elementary particles, building blocks of our visible Universe, and interactions between them. These elementary particles possess intrinsic properties such as electric charge ( $Q$ ), mass, and spin. One subset of these elements, the quarks, also carry color charge and are subject to the strong interaction mediated by gluons, as described by Quantum Chromodynamics (QCD).

Conventionally, quarks are believed to carry a baryon number of  $B = 1/3$ . Therefore, three quarks combine to form a baryon with  $B = 1$ , while a quark-antiquark pair form a meson with  $B = 0$ . Meanwhile, an alternative picture was proposed in early 1970s (3, 4), which stipulates that valence quarks are connected by gluons in a Y-shaped topological structure, called the baryon (or gluon) junction. It is this topological configuration of the gluons that is posited to trace the baryon number. Such a junction structure obeys the fundamental physics conservation laws and does not contradict any existing observations (4, 5). Although it is not possible to compute such an object with perturbative quark and gluon interactions, it has been studied in

Lattice QCD (6–8). The top-left panel of Fig. 1 illustrates a baryon with three valence quarks each carrying  $B = 1/3$  and  $Q \neq 0$ , while the bottom-left panel illustrates the alternative picture of a baryon junction carrying  $B = 1$  and  $Q = 0$ . The three ends of the baryon junction are connected to valence quarks with few exceptions (9, 10), making it indistinguishable for most physical processes whether the junction or valence quarks carry the baryon number (5, 9). For this reason, neither scenario for what carries the baryon number has been unequivocally verified experimentally to date. The few exceptions of junction connections without valence quarks include possible configurations of baryonium tetraquarks (10), exotic gluonic states of junction and anti-junction such as baryonium glueballs, gluonic graphene and buckyballs (9). None of these configurations has been discovered by experiments so far.

The phenomenon of “baryon transport” in high-energy nuclear collisions, referring to the way the baryon number is moved around in the momentum space, provides a potential tool to identify the carrier of the baryon number (5, 11, 12). In these collisions, significant excesses of baryons over antibaryons have been observed at mid-rapidity<sup>1</sup> ( $y \sim 0$ ) in the center-of-mass frame (12–15). Due to baryon number conservation, these excess baryons must contain the baryon numbers that get transported from the colliding nuclei at beam rapidity ( $y = \pm Y_{\text{beam}}$ ) to mid-rapidity. The right panels of Fig. 1 illustrate how the baryon number can be transported out of a colliding baryon at  $Y_{\text{beam}}$  for either valence quarks (top) or baryon junctions (bottom). In the valence quark picture, multiple valence quarks need to be transported to form baryons around mid-rapidity, while in the junction picture, a junction can be transported to mid-rapidity and coupled with quarks from quark-antiquark pairs popping out of vacuum to form baryons. There is a key difference between the two mechanisms, namely that valence quarks, which carry a large fraction of the colliding baryon’s momentum, are difficult to transport from  $Y_{\text{beam}}$  to  $y \sim 0$ , while baryon junctions, composed of low-momentum gluons, are easier to be transported to mid-rapidity. Therefore, one expects enhanced baryon transport for the junction picture compared to that of the valence quark picture. These general arguments are supported by the state-of-the-art Monte Carlo simulation (PYTHIA (16–18) and HERWIG (19)) even in proton+proton ( $p+p$ ) collisions, where different versions of PYTHIA show that valence quark transports are not sufficient to produce the baryon excess observed in high-energy  $p+p$  collisions and the formation of baryon junctions through color reconnection of strings would enhance the baryon transport.

The STAR Collaboration at the Relativistic Heavy Ion Collider (RHIC) presents three independent approaches to investigate the question of what carries the baryon number (11). First, we study charge and baryon transport to mid-rapidity, utilizing the dataset from isobar  $^{96}_{44}\text{Ru}+^{96}_{44}\text{Ru}$  and  $^{96}_{40}\text{Zr}+^{96}_{40}\text{Zr}$  collisions (20). Second, we measure the rapidity dependence of proton, antiproton and net-proton (proton minus antiproton) yields in photon-gold ( $\gamma+\text{Au}$ ) interactions (21). Third, we point out that previously measured net-proton yields at mid-rapidity from Au+Au collisions of different energies (15, 22) show a striking exponential scaling as a function of the rapidity shift from  $Y_{\text{beam}}$  to  $y \sim 0$  (11). These results are compared with theoretical expectations

---

<sup>1</sup>Rapidity is defined as  $y = \frac{1}{2} \ln \frac{E+p_z c}{E-p_z c}$ , where  $E$  and  $p_z$  are the energy and the  $z$  component of momentum along beam direction for a particle while  $c$  is the speed of light.

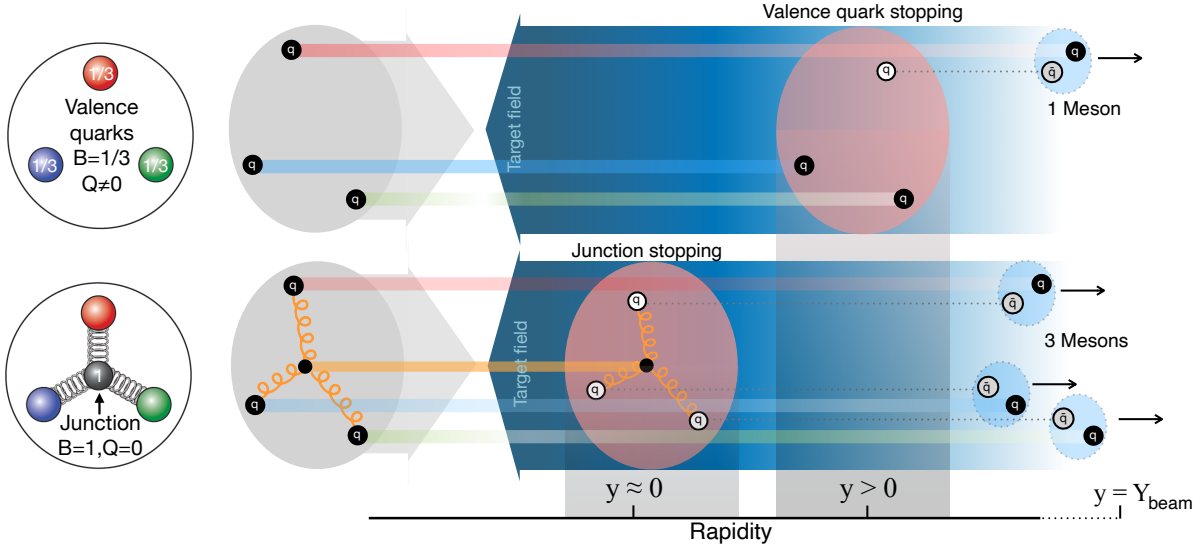


Figure 1: **Baryon number carrier and transport mechanism.** Left: illustration of two possible carriers of the baryon number (top: valence quarks; bottom: baryon junction). Right: transport of baryon number in high-energy collisions from beam rapidity ( $y = Y_{\text{beam}}$ ), if carried by the valence quarks (top) or the baryon junction (bottom). Unstopped valence quarks (solid black circles) can form mesons close to beam rapidity. Open circles represent produced quarks and anti-quarks.

based on valence quarks or baryon junction scenarios.

## Baryon transport vs. charge transport

In high-energy nucleus-nucleus collisions, charge and baryon numbers, carried by colliding nuclei at  $Y_{\text{beam}}$ , can be transported to other rapidities due to strong interactions. To experimentally quantify the charge and baryon number transport to a specific rapidity, we measure net-charge ( $Q$ ) and net-baryon ( $B$ ) numbers at that rapidity. They are defined as:

$$Q = (N_{\pi^+} + N_{K^+} + N_p) - (N_{\pi^-} + N_{K^-} + N_{\bar{p}}) \quad (1)$$

and

$$B = (N_p + N_n) - (N_{\bar{p}} + N_{\bar{n}}). \quad (2)$$

Here,  $N_{\pi^+}$ ,  $N_{K^+}$ ,  $N_p$  are the yields of positively charged pions ( $\pi$ ), kaons ( $K$ ) and protons ( $p$ ), while  $N_{\pi^-}$ ,  $N_{K^-}$ , and  $N_{\bar{p}}$  denote their antiparticles (23).  $N_n$  and  $N_{\bar{n}}$  are the yields of neutrons and antineutrons.

Since valence quarks are known to carry electric charge (24, 25), in the scenario of valence quarks also carrying the baryon number, the ratio of baryon and charge numbers ( $B/Q$ ) transported to mid-rapidity is expected to be equal to  $A/Z$  in the absence of any other effects, where

$Z$  and  $A$  are the atomic and mass numbers of the colliding nuclei. For the alternative scenario of the baryon junction as the carrier, one expects  $B/Q > A/Z$  since junction carries zero electric charge and one unit of baryon number, and can be transported by strong interactions. Since the small net-charge number is determined from the difference between large yields of positively and negatively charged particles, as illustrated in Eq. 1, measuring charge transport in one species of nuclear collisions usually involves large uncertainties and thereby making it impossible to date to achieve the necessary experimental precision. This challenge is mitigated in our study by evaluating the difference in the charge transport ( $\Delta Q$ ) between two isobar collision species ( $^{96}_{44}\text{Ru}+^{96}_{44}\text{Ru}$  and  $^{96}_{40}\text{Zr}+^{96}_{40}\text{Zr}$ ), recorded by the STAR experiment (26) in 2018, via double ratios:

$$\Delta Q = Q_{\text{Ru+Ru}} - Q_{\text{Zr+Zr}} \approx N_{\pi}(R2_{\pi} - 1) + N_K(R2_K - 1) + N_p(R2_p - 1), \quad (3)$$

where  $N_{\pi}$ ,  $N_K$ , and  $N_p$  are the average yields over positively and negatively charged hadrons and over Ru+Ru and Zr+Zr collisions.  $R2_{\pi} = (N_{\pi^+}/N_{\pi^-})_{\text{Ru+Ru}}/(N_{\pi^+}/N_{\pi^-})_{\text{Zr+Zr}}$  is the double ratio for pions, and  $R2_K$  and  $R2_p$  are defined similarly for kaons and protons (11). These double ratios, which deviate from unity on the order of  $10^{-3}$  (23), can be measured precisely with negligible uncertainties since the Ru and Zr data were taken with almost identical accelerator and detector conditions (20) and analyzed with the same procedure. Then the ratio  $\langle B \rangle / \Delta Q$  is compared against  $A / \Delta Z$ , where  $\langle B \rangle$  is the average net-baryon number in Ru+Ru and Zr+Zr collisions,  $\Delta Z = 4$  and  $A = 96$ . As a reminder, one expects  $\langle B \rangle / \Delta Q \approx A / \Delta Z$  in the valence quark picture, and  $\langle B \rangle / \Delta Q > A / \Delta Z$  in the junction picture.

The STAR experiment recorded about 2 billion Ru+Ru and Zr+Zr collision events each at a center-of-mass energy per nucleon-nucleon pair ( $\sqrt{s_{\text{NN}}}$ ) of 200 GeV. Yields of positively and negatively charged  $\pi$ ,  $K$ ,  $p$ , as well as the double ratios ( $R2_{\pi}$ ,  $R2_K$ , and  $R2_p$ ) are measured as a function of transverse momentum ( $p_{\text{T}}$ ) within  $|y| < 0.5$  in five centrality classes (23). Here, centrality refers to the geometric overlap between the two colliding nuclei, with central (peripheral) events referring to those with small (large) impact parameters, the distance between the centers of the colliding nuclei at the time of overlap. These yields consist of primordial production from the collision zone as well as secondary products from resonance and weak decays. Neutrons cannot be measured by the STAR detector, therefore, their yields have to be estimated. The primordial production is determined based on the measured proton yields and antideuteron-to-deuteron ratios ( $\bar{d}/d$ ), while the decay or feed-down contribution, contributing to approximately 30% of the total neutron yield, is estimated from hyperon yields and known branching ratios (23). The same procedure is applied to estimate the yields for antineutrons (23). The yield distributions and double ratios are fit with a Blast-wave function (27) and a linear function, respectively, to extrapolate from the measured to the full  $p_{\text{T}}$  range.  $\langle B \rangle$  and  $\Delta Q$  are calculated in individual  $p_{\text{T}}$  bins using the measured data or extrapolated values, and then integrated to obtain the final reported values. Since the used particle yields include decay contributions, the above calculated  $\langle B \rangle$  and  $\Delta Q$  values closely approximate the true net-baryon and net-charge numbers with a relative error of 1% or less due to unmeasured nuclei.

Figure 2 shows the resulting  $\langle B \rangle / \Delta Q$ , multiplied by  $\Delta Z / A$ , as a function of centrality at

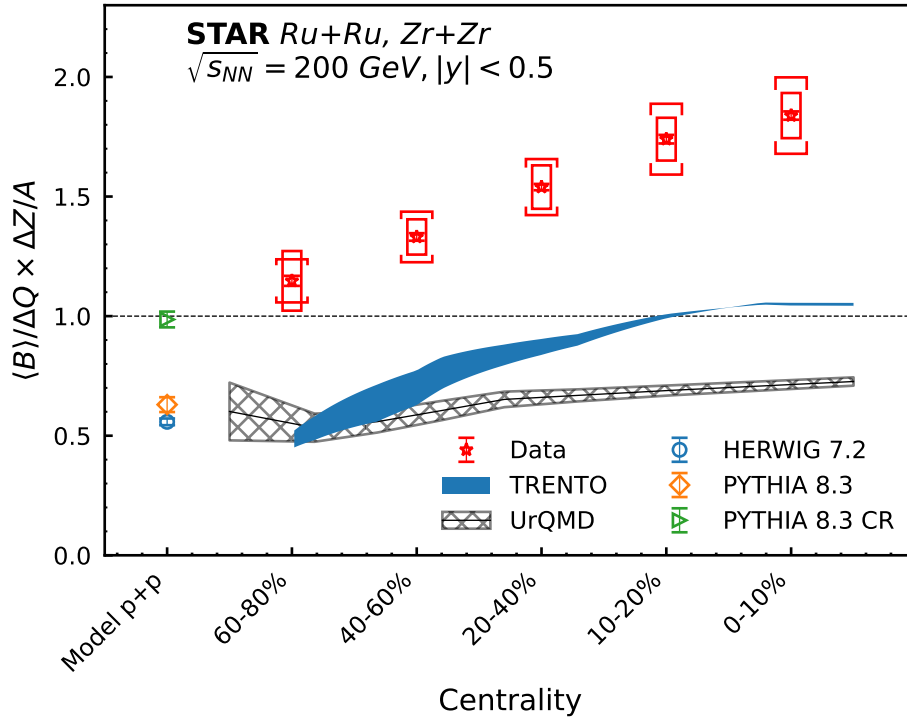


Figure 2: **Baryon to charge transport ratio.** The ratio of the mean net-baryon number ( $\langle B \rangle$ ) to the net-charge difference between Ru+Ru and Zr+Zr collisions ( $\Delta Q$ ), scaled by  $\Delta Z/A = 4/96$ , as a function of centrality. Red stars represent data with the boxes (vertical bars) around them representing systematic (statistical) uncertainties. Uncertainties arising from estimations of feed-down contributions to neutrons and antineutrons are shown separately as brackets. The horizontal dashed line at 1 shows the naive expectation if the baryon number is carried by valence quarks and all other effects are ignored. Model calculations from UrQMD (hatched band) (28, 29), TRENTO (solid band) (30), PYTHIA 8.3 (diamond) (16), PYTHIA 8.3 with Color Reconnection Mode 2 (triangle) (19) are also shown for comparison. See text for details.

mid-rapidity ( $|y| < 0.5$ ), corresponding to an average rapidity shift of 5.36. In 0-10% most central collisions,  $\langle B \rangle / \Delta Q \times \Delta Z / A = 1.84 \pm 0.02$  (stat.)  $\pm 0.09$  (syst.)  $\pm 0.16$  (feed-down), much larger than the naive expectation of unity for the scenario of valence quarks carrying the baryon number. Larger baryon transport compared to charge transport is consistent with the expectation of the baryon junction scenario. The ratio decreases monotonically from 0-10% most central to 70-80% peripheral collisions. A similar decreasing trend is seen in the TRENTO model calculation (30), which estimates  $\langle B \rangle / \Delta Q$  using the number of protons and neutrons participating in the collision without simulating any system evolution after the initial collision interactions. Such a trend is attributed to the larger neutron skin for the Zr nucleus

than that for Ru, which results in an increasingly smaller fraction of participating protons in Zr+Zr collisions compared to Ru+Ru as the collisions become more peripheral. The width of the band for the TRENTO calculation corresponds to the uncertainty in the neutron skin values used. More sophisticated calculations based on the Ultra relativistic Quantum Molecular Dynamics (UrQMD) (28, 29), which simulates the entire evolution of nuclear collisions, and can reproduce the net-baryon yields in central Ru+Ru and Zr+Zr collisions (23), are also shown for comparison. UrQMD does not include baryon junctions and predicts a value of 0.5 to 0.7, significantly below the experimental data. Another heavy-ion model, A MultiPhase Transport (AMPT) (31) model, predicts even smaller ratios than UrQMD (11). This ratio is also smaller than the naive expectation of unity, due to an excess of anti-strange quarks over strange quarks at mid-rapidity in the simulation. The neutron skin effect is not included in the UrQMD calculation, hence it does not exhibit the significant increasing trend from peripheral to central collisions discussed above. The limiting case of  $p+p$  collisions at  $\sqrt{s} = 200$  GeV is simulated with three event generators: HERWIG 7.2 (default tune) (19), PYTHIA 8.3 (default tune) (17), and PYTHIA 8.3 with Color Reconnection (CR) Mode 2 (16, 17), all of which assume valence quarks as the carriers of the baryon number and do not include junctions in the colliding protons. HERWIG 7.2 employs a quark-diquark model for baryon production, while PYTHIA 8.3 (default tune) produces baryons mainly through the so-called “popcorn” mechanism (18). Both models predict  $B/\Delta Q$  values between 0.5-0.6. On the other hand, PYTHIA 8.3 CR allows the dynamical formation of baryon junctions through color reconnection prior to hadronization, thus enhancing baryon production at mid-rapidity.  $B/\Delta Q$  increases to  $0.99 \pm 0.03$  compared to the PYTHIA 8.3 default tune. We note that while the number of participating nucleons for peripheral Ru+Ru and Zr+Zr collisions is close to that of  $p+p$  collisions, the peripheral data is affected by the aforementioned neutron skin effect and should not be directly compared to HERWIG and PYTHIA predictions.

## Baryon transport along rapidity

Exploring the dependence of baryon transport on rapidity can also shed light on the identity of the baryon number carrier. In particular, photon-induced interactions (21) on nuclei provide a clean environment to study the baryon transport as the incoming photon does not carry any baryon number. In such interactions, the rapidity dependence of the net-baryon yield is expected to follow an exponential distribution (5):

$$f(y) \propto \exp(-\alpha_B \Delta y), \quad (4)$$

where  $\Delta y = Y_{\text{beam}} - y$ . For a given beam energy ( $Y_{\text{beam}}$ ), the rapidity dependence becomes  $f(y) \propto \exp(\alpha_B y)$ . The slope parameter ( $\alpha_B$ ) is predicted to be within  $0.42 < \alpha_B < 1$  by the baryon junction framework (5). The upper and lower limits correspond to junction-junction (J + J) and junction-Pomeron (J +  $\mathbb{P}$ ) interactions, where a Pomeron is a theorized two-gluon configuration. This predicted  $\alpha_B$  range also applies to baryon transport in hadron-hadron collisions (5), as discussed later.

The photon-induced processes used in this analysis are inclusive  $\gamma$ +Au interactions selected from Au+Au collisions at  $\sqrt{s_{\text{NN}}} = 54.4$  GeV. In such collisions, quasi-real photons with an average energy of  $E_\gamma \simeq 0.8$  GeV are emitted from the projectile Au ion and interact with the target Au ion possessing an energy of 27.2 GeV per nucleon (32–34). This results in an average center-of-mass energy of  $W_{\gamma N} \sim 9$  GeV for the photon-nucleon system (11). The  $\gamma$ +Au events are selected by exploiting their characteristic asymmetric rapidity distribution of particle production and the differing neutron distributions of the target and projectile nuclear remnants (23).

Yields of protons and antiprotons as a function of  $m_T - m_p$ , where  $m_p$  is the proton mass and  $m_T = \sqrt{p_T^2 + m_p^2}$ , are measured in twelve different rapidity intervals (23). The net-proton yield is calculated as a proxy to quantify the baryon transport. In order to extract the total yields, proton, antiproton and net-proton spectra are parameterized and extrapolated to unmeasured regions (23). Left panel of Fig. 3 shows the proton, antiproton and net-proton rapidity

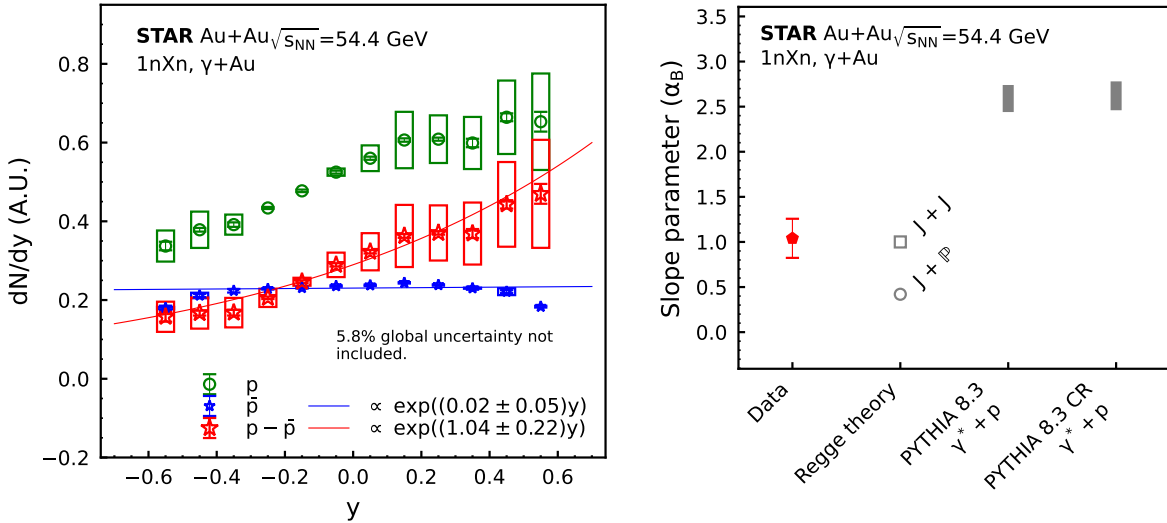


Figure 3: **Baryon transport in  $\gamma$ +Au interactions.** Left: proton, antiproton, and net-proton rapidity densities ( $dN/dy$ ) in  $\gamma$ +Au events selected from Au+Au collisions at  $\sqrt{s_{\text{NN}}} = 54.4$  GeV. The selection requires remnants of a single neutron ( $1n$ ) in the  $\gamma$ -going direction (negative  $y$ ) and more than one neutron ( $Xn$ ) in the Au-going direction (positive  $y$ ). Fit results with an exponential function to antiproton and net-proton distributions are shown as solid curves. Right: comparison of the exponential slope parameter in  $\gamma$ +Au events to those from Regge theory predictions assuming baryon junction (5) as well as from  $\gamma^*+p$  events simulated using the PYTHIA 8.3 default and CR tunes.

densities ( $dN/dy$ ) in  $\gamma$ +Au events within  $|y| < 0.6$  in the lab frame. The efficiency for selecting  $\gamma$ +Au events is not accounted for. This missing normalization factor does not affect the

extracted rapidity slopes but our reported absolute yields cannot be directly compared to theoretical calculations. In this figure, results from events where the photon travels in the negative  $y$  direction are plotted unchanged, while those from the reversed collision kinematics are reflected around  $y = 0$  and added. This is because  $\gamma$ +Au events are selected from Au+Au collisions and either Au nucleus can emit the photon. Both the proton and net-proton  $dN/dy$  have positive slopes with respect to  $y$ . It is worth noting that the antiproton rapidity distribution is mostly flat against  $y$  with an exponential slope close to zero, *i.e.*,  $\alpha_{\bar{B}} = 0.02 \pm 0.05$ . This is consistent with theoretical expectations of a weaker rapidity dependence for proton-antiproton pair production, the sole production mechanism for antiproton, than for baryon transport (5, 21), and is a clear demonstration that the strong rapidity dependence of the net-proton yield is not due to the  $\gamma$ +Au event selection. A fit to the net-proton rapidity density with Eq. (4) and  $Y_{\text{beam}} = 4.06$  gives  $\alpha_B = 1.04 \pm 0.22$ . As shown in the right panel of Fig. 3,  $\alpha_B$  for  $\gamma$ +Au events is consistent with the Regge theory prediction incorporating the baryon junction (5). On the other hand,  $\gamma^*+p$  events with kinematics constrained to be similar to those of the  $\gamma$ +Au events used in this analysis are simulated with PYTHIA 8.3 default and CR tunes (16). Specifically, the colliding protons have a beam energy of 27 GeV and the virtual photon kinematics are limited to  $Q^2 < 0.01$  (GeV/c)<sup>2</sup> and  $E_\gamma < 2$  GeV. Both tunes are seen to significantly overpredict the measured slope for  $\gamma$ +Au events.

We now shift our focus to baryon transport along rapidity in hadronic processes. An exponential dependence of the net-proton yield on  $\Delta y$  is also observed in Au+Au collisions (11). In this case of symmetric collisions, the dependence of net-proton yields at mid-rapidity, measured over a large range of beam energy ( $\sqrt{s_{\text{NN}}} = 7.7 - 200$  GeV) (15, 22), on  $\Delta y = Y_{\text{beam}} - y$  are fit with Eq. (4). In this study, the measurements are made at  $y \sim 0$ , while  $Y_{\text{beam}}$  varies with beam energy. This procedure is followed in Ref. (11), and the resulting  $\alpha_B$  as a function of centrality is shown in Fig. 4. It is independent of collision centrality with an average value of  $0.64 \pm 0.05$  (11). This is consistent with the slope parameter for  $\gamma$ +Au processes within  $1.7\sigma$ . Please note that  $\alpha_B$  could depend on collision kinematics as predicted in (3, 21), but our current measurements in Au+Au and  $\gamma$ +Au events are not sufficient to draw firm conclusions on such kinematics dependence.

Figure 4 also includes the predicted slopes from the Regge theory for the baryon junction, which encompass the Au+Au data. Slope parameters from UrQMD simulations of Au+Au collisions and from PYTHIA and HERWIG simulations of  $p+p$  collisions (11) are extracted the same way as for the Au+Au data and shown for comparison. Contrary to that observed in data,  $\alpha_B$  decreases by about 0.1 from peripheral to central collisions in UrQMD, consistent with the expectation for the valence quark transport that gets enhanced by increasing multiple scatterings with centrality (peripheral to central) and/or collision energy (35). The Au+Au data is consistent with PYTHIA 8.3 CR tune, but not with either the PYTHIA 8.3 default tune or Herwig 7.2. This indicates that the implementation of dynamical baryon junction formation in PYTHIA 8.3 CR tune, a partial imitation of the baryon junction mechanism, does improve agreement with data. However, both tunes of PYTHIA 8.3 overpredict the measured slope for  $\gamma$ +Au events, possibly due to a lack of certain physics ingredients in the model. A full implementation of the baryon

junction mechanism (3–5) by including baryon junctions in the incoming protons and junction scatterings could potentially improve the agreement between data and modeling.

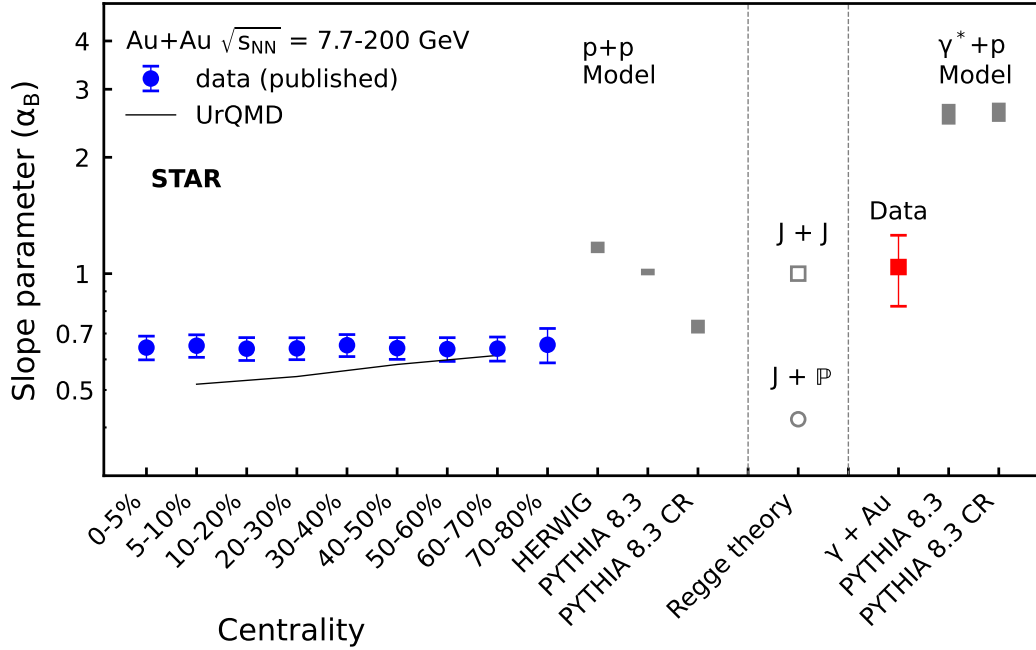


Figure 4: **Rapidity slope of baryon transport.** The exponential slopes of the net-proton  $dN/dy$  vs.  $\Delta y$  in different centrality intervals of Au+Au collisions (11, 15, 22). They are compared to those from  $\gamma$ +Au events and various predictions. Vertical bars around experimental data points represent combined statistical and systematic uncertainties.

## Discussions and outlook

We have reported new measurements from isobar and  $\gamma$ +Au collisions with the STAR detector that investigate whether the carrier of the baryon number is valence quarks or alternative topological entities such as the baryon junction. These results, supported by data previously reported by STAR from Au+Au collisions at a variety of beam energies, disfavor the valence quark picture. Further investigation is needed to explore alternative theories, but for them to be viable, they should simultaneously account for all the phenomena, an achievement that currently appears to be possible with the baryon junction picture.

Future measurements at the Electron-Ion Collider at the same nuclear kinematics with similar net-baryon yield and rapidity acceptance as our measurements will further shed light on the nature of the baryon number carrier and directly probe its distribution function in nuclei (11, 36, 37).

## Acknowledgments

We thank the RHIC Operations Group and RCF at BNL, the NERSC Center at LBNL, and the Open Science Grid consortium for providing resources and support. This work was supported in part by the Office of Nuclear Physics within the U.S. DOE Office of Science, the U.S. National Science Foundation, National Natural Science Foundation of China, Chinese Academy of Science, the Ministry of Science and Technology of China and the Chinese Ministry of Education, the Higher Education Sprout Project by Ministry of Education at NCKU, the National Research Foundation of Korea, Czech Science Foundation and Ministry of Education, Youth and Sports of the Czech Republic, Hungarian National Research, Development and Innovation Office, New National Excellency Programme of the Hungarian Ministry of Human Capacities, Department of Atomic Energy and Department of Science and Technology of the Government of India, the National Science Centre and WUT ID-UB of Poland, the Ministry of Science, Education and Sports of the Republic of Croatia, German Bundesministerium für Bildung, Wissenschaft, Forschung and Technologie (BMBF), Helmholtz Association, Ministry of Education, Culture, Sports, Science, and Technology (MEXT), Japan Society for the Promotion of Science (JSPS) and Agencia Nacional de Investigación y Desarrollo (ANID) of Chile.

# 1 Materials and Methods

## 1.1 Charge and baryon transport in Ru+Ru and Zr+Zr collisions

Ru+Ru and Zr+Zr collisions recorded by the STAR experiment are utilized for comparing charge and baryon transport.

### 1.1.1 Invariant yields of charged particles

Ru+Ru and Zr+Zr events are retained if their collision vertices are between -35 cm and +25 cm along the beam direction and within 2 cm along the radial direction with respect to the nominal center of the STAR detector. Invariant yields of  $\pi$ ,  $K$ ,  $p$ , and  $d$  as a function of transverse momentum ( $p_T$ ) in different centrality classes are measured utilizing the Time Projection Chamber (TPC) (38) and the Time-Of-Flight (TOF) detector (39). The event centrality is classified by fitting the distribution of charged particle multiplicity within the pseudorapidity range of  $|\eta| < 0.5$  with the Monte Carlo Glauber model (20). Central (peripheral) events correspond to those with large (small) multiplicities and large (small) number of participating nucleons ( $\langle N_{\text{part}} \rangle$ ). The TPC is a gaseous detector, which tracks the trajectories of traversing charged particles. TPC tracks are accepted if there are at least 15 TPC space points used for track reconstruction, and each track has a Distance of Closest Approach (DCA) to the collision vertex less than 3 cm. Furthermore, the ratio of the number of used TPC space points to the maximum possible number along the track trajectory is required to be at least 0.52 to remove split tracks. The kinematic coverage of the measurement is  $0.2 < p_T < 2.5$  GeV/ $c$  for  $\pi$  and  $K$ ,  $0.45 < p_T < 2.5$  GeV/ $c$  for  $p$ , and  $0.9 < p_T < 4.2$  GeV/ $c$  for  $d$ , within the rapidity range of  $|y| < 0.5$  for all species.

Charged particles lose energy in the TPC through ionizing gas atoms, and the amount of energy loss ( $dE/dx$ ) depends on the particle mass, which can be used for identifying the particle species. The variable  $n\sigma_i = (\ln(dE/dx)_{\text{measured}} - \ln(dE/dx)_{i,\text{expected}}) / R(\ln(dE/dx))$  is used, where  $(dE/dx)_{\text{measured}}$  is the measured energy loss in the TPC,  $(dE/dx)_{i,\text{expected}}$  is the expected energy loss for particle  $i$  based on the Bichsel formalism (40), and  $R(\ln(dE/dx))$  is the experimental resolution of  $\ln(dE/dx)$ . To ensure good resolution, each track should have at least 10 TPC space points used for calculating  $dE/dx$ . Since the particle identification capability of the TPC is limited to low  $p_T$ , it is used up to 0.5 GeV/ $c$ , 0.25 GeV/ $c$ , and 0.7 GeV/ $c$  for  $\pi$ ,  $K$ ,  $p$ , respectively, above which the TOF is used. For the  $d$  measurement, the TOF is always used. The raw yield for particle  $i$  in a given  $p_T$  bin is extracted by counting the entries under the peak of particle  $i$  in the  $n\sigma_i$  distribution within  $[\mu_i - 2\sigma_i, \mu_i + 2\sigma_i]$ .  $\mu_i$  and  $\sigma_i$  are the mean and width of the signal peak, determined by fitting the  $n\sigma_i$  distribution with a multi-Gaussian function. The missing yield outside the counting range is corrected for based on the fitted Gaussian function shape. To minimize the uncertainties in measuring the double ratios, the  $n\sigma_i$  distribution for negatively charged particles in Ru+Ru collisions is fit first, and the resulting mean and width values for the various Gaussian distributions are used to fix the corresponding parameters when fitting positively charged particles in Ru+Ru collisions and particles of both charges in Zr+Zr collisions.

As aforementioned, the TOF is used for identifying  $\pi$ ,  $K$ ,  $p$ , at higher  $p_T$  ranges. Based on the arrival time ( $t_f$ ) measured in the TOF, the collision start time ( $t_0$ ) measured in the Vertex Position Detectors (VPDs) (41), the momentum ( $p$ ) from the TPC, and the trajectory length ( $L$ ) from collision vertex to TOF, one can calculate the particle's mass squared:  $m^2 = p^2[c^2(t_f - t_0)^2/L^2 - 1]$ , where  $c$  is the speed of light. A fit to the  $m^2$  distribution in each  $p_T$  bin is performed using three Student's  $t$ -distributions, representing the three particle species, and the raw yields are obtained directly from the fit. Since the deuteron peak in the  $m^2$  distribution is far away from other particles, a single student's  $t$ -distribution describing the signal plus an exponential function representing the background are used for fitting. The  $d$  yields are also taken from the fit. As for the case of  $n\sigma_i$  fitting, the shape parameters for negative particles in Ru+Ru collisions are used to fix the functional shapes for other cases while the yields are left as free parameters.

Corrections for the tracking efficiency and energy loss in the TPC are evaluated using the embedding technique, where simulated particles of interest are propagated through the GEANT 3 (42) simulation of the STAR detector, mixed with real events and reconstructed the same way as data. The TOF matching efficiency correction is estimated with a data-driven method, and applied to account for the efficiency of the TOF detector in detecting tracks previously measured by the TPC. Additional protons can be knocked out of the detector material by high- $p_T$  hadrons, and thus need to be subtracted. Their contribution is estimated by fitting the DCA distribution for the measured proton sample with two components: one for the signal protons using the DCA distribution for antiprotons which do not suffer from knock-out contamination, and the other for the background protons parameterized with a functional shape. A similar procedure is applied to subtract knock-out deuterons from the measured sample. For the (anti-) $d$  measurement, an additional absorption correction is applied to account for the overestimation of the (anti-) $d$  tracking efficiency due to GEANT 3 lacking the correct (anti-) $d$  interaction cross section in detector material (43, 44).

Fully corrected invariant yields of  $\pi$ ,  $K$ ,  $p$ , and  $d$  within  $|y| < 0.5$  are shown in Fig. S1 as a function of  $p_T$  ( $p_T/2$  for  $d$ ) for Ru+Ru and Zr+Zr collisions at  $\sqrt{s_{NN}} = 200$  GeV, respectively. Decay daughters of resonances and weak-decaying particles are included in the measured yields. Spectra in different centrality classes are scaled vertically with arbitrary factors for visual clarity. Vertical bars and boxes around data points, which are smaller than the marker size in most cases, represent statistical and systematic uncertainties. Systematic uncertainties on the yields include those originating from signal extraction, missing yields from weak decays due to the finite DCA cut of 3 cm, imperfect simulation of the detector response and, for the case of the proton measurement, the estimated knock-out background in the detector material. Dashed curves crossing data points indicate fits to the measurements with a Blast-wave function (27).

Double ratios of  $\pi$ ,  $K$ , and  $p$  ( $R2_\pi$ ,  $R2_K$ ,  $R2_p$ ) between positively and negatively charged particles and between Ru+Ru and Zr+Zr collisions are shown in Fig. S2 as a function of  $p_T$  in five different centrality classes. Only statistical uncertainties are displayed as the systematic uncertainties are negligible due to the cancellation of detector effects. Solid curves illustrate fits to the double ratios with a first-order polynomial function for extrapolating to both lower and higher  $p_T$ . Bands around solid lines represent the uncertainties on the fits originating from the

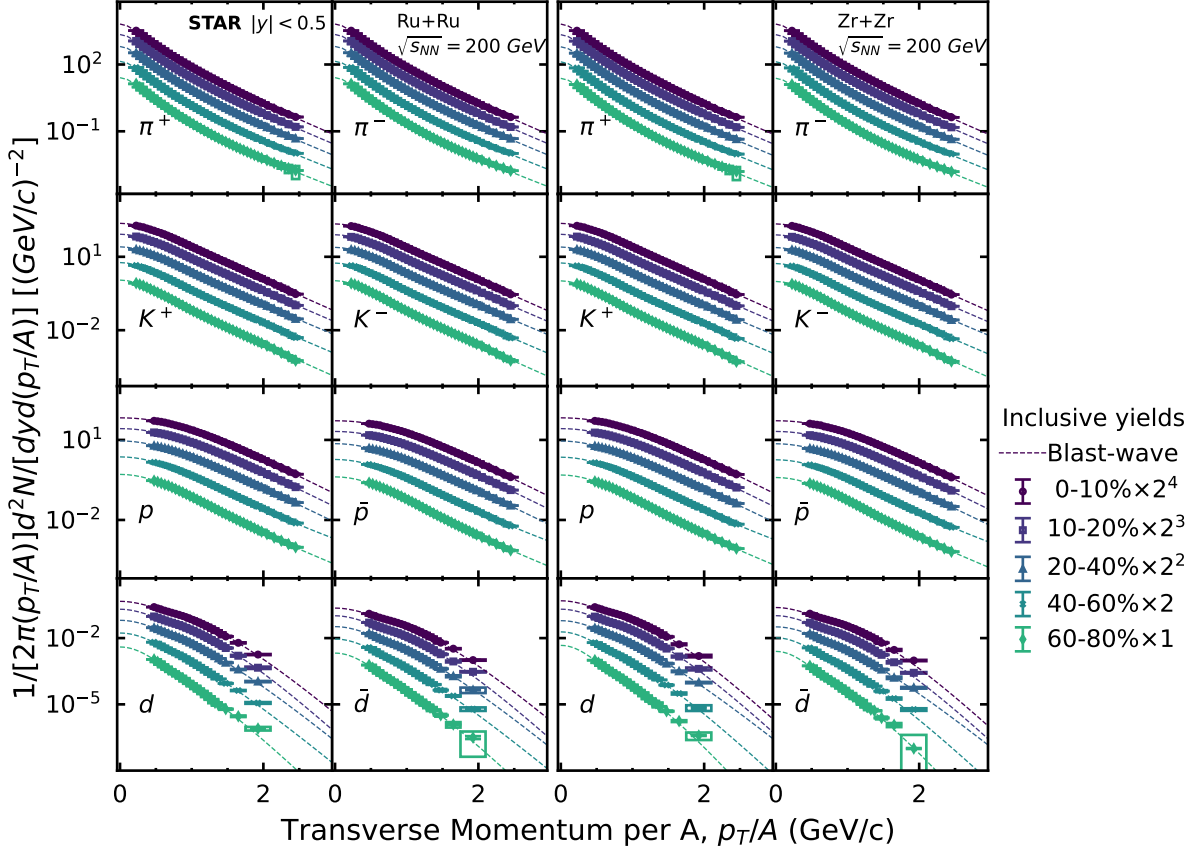


Figure S1: **Identified particle spectra.** Identified particle spectra, including all decay contributions, within  $|y| < 0.5$  in Ru+Ru (left two columns) and Zr+Zr (right two columns) collisions at  $\sqrt{s_{NN}} = 200$  GeV. From top to the bottom, the particles being plotted are pions, kaons, protons and deuterons, respectively. The  $x$ -axis,  $p_T/A$ , is the transverse momentum per nucleon. For simplicity,  $A = 1$  for pions and kaons even though they are not nucleons. For both the Zr and Ru cases, the left column shows positively charged particles, and the right shows negatively charged particles. The vertical error bar size represents the statistical uncertainty while the box height represents the systematic uncertainty. The dashed curves show the fitted Blast-wave function (27).

statistical errors of the double ratios. Additional uncertainties arising from the extrapolation of double ratios to low and high  $p_T$  in calculating the charge number are evaluated by changing the fit function to either a zeroth-order or a second-order polynomial function. Furthermore, impact of knock-out protons on the proton double ratio measurement is also included as a source of uncertainties.

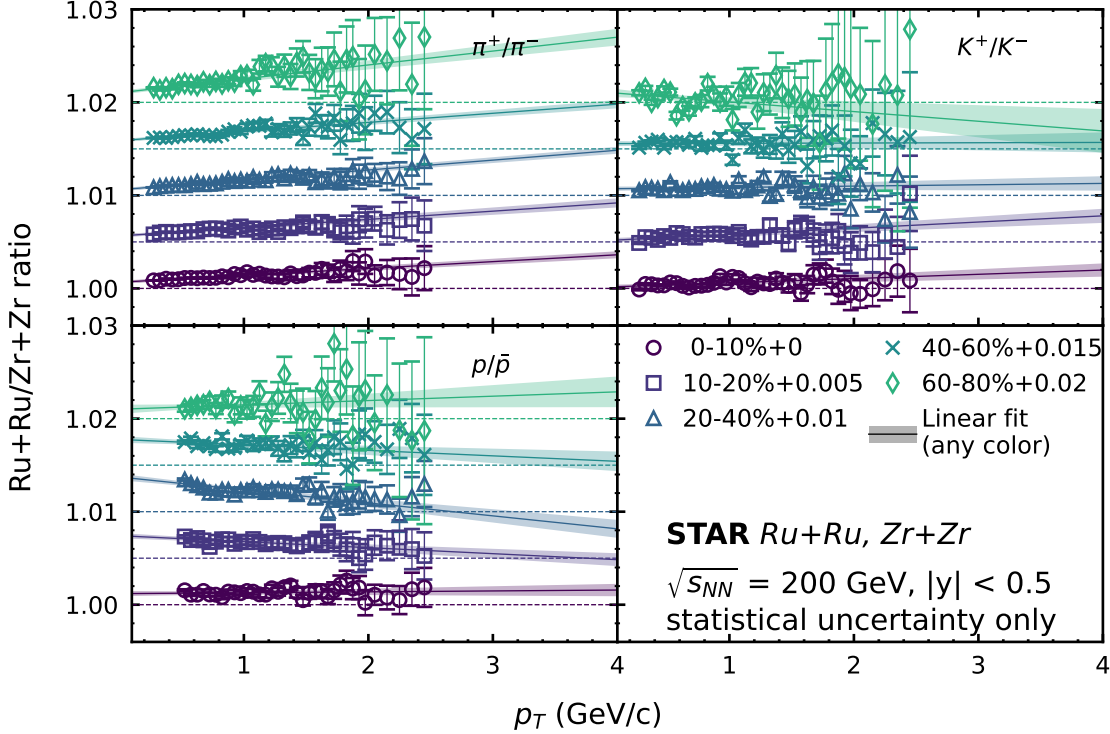


Figure S2: **Particle yield double ratios.** Double ratios of  $\pi$ ,  $K$ , and  $p$  between positively and negatively charged particles and between Ru+Ru and Zr+Zr collisions at  $\sqrt{s_{NN}} = 200$  GeV. Horizontal dashed lines display offsets for each centrality class, while solid lines with shaded error bands represent fits to the double ratios with a first-order polynomial function.

### 1.1.2 Derivation of neutron and antineutron yields

Neutrons make up a large fraction of baryons at mid-rapidity. However, they are not directly measured by the STAR detector, so their yields need to be estimated. The neutron yield ( $N_n^{\text{inc}}$ ) consists of primordial production ( $N_n^{\text{pri}}$ ) and feed-down contribution from decays of hyperons ( $N_n^{\text{FD}}$ ), which are baryons with at least one strange valence quark, *i.e.*,

$$N_n^{\text{inc}} = N_n^{\text{pri}} + N_n^{\text{FD}}. \quad (5)$$

The feed-down contribution to the neutron yield is estimated based on the yields of hyperons:

$$N_n^{\text{FD}} = 0.361(N_\Lambda + N_{\Xi^0} + N_{\Xi^-} + N_\Omega) + 0.4831N_{\Sigma^+} + N_{\Sigma^-}, \quad (6)$$

where the numeric factors represent branching ratios to neutrons (45) and the subscript of  $N$  shows which hyperon species the yield corresponds to. Since  $\Sigma^0$  decays 100% to  $\Lambda$  electromagnetically and is indistinguishable from  $\Lambda$  experimentally (46), its yield is considered part of the  $\Lambda$  yield ( $N_\Lambda$ ). The hyperon yields are derived based on the experimental measurement of feed-down contribution to protons as well as model calculations. Feed-down contributions to the proton sample can be written as:

$$N_p^{\text{FD}} = 0.639(N_\Lambda + N_{\Xi^0} + N_{\Xi^-} + N_\Omega) + 0.5157N_{\Sigma^+}. \quad (7)$$

The fraction of protons that comes from feed-down has been evaluated as a function of  $\langle N_{\text{part}} \rangle$  for Au+Au collisions at  $\sqrt{s_{\text{NN}}} = 200$  GeV using a data-driven method (47), and is extrapolated to the  $\langle N_{\text{part}} \rangle$  values of Ru+Ru and Zr+Zr collisions used in this analysis.  $N_p^{\text{FD}}$  is equal to the observed proton yields in Ru+Ru and Zr+Zr collisions multiplied by the extrapolated feed-down fraction. The yield ratios of different hyperons to that of  $\Lambda$  are calculated using the THERMUS thermal model (48), whose parameters are fitted to the yields of pion, kaon, proton, their antiparticle counterparts as well as the antideuteron-to-deuteron ratios measured in Ru+Ru and Zr+Zr collisions. With these, yields for all hyperons can be evaluated using Eq. (7), and  $N_n^{\text{FD}}$  is then estimated by Eq. (6).

In the framework of the statistical thermal model and under Boltzmann approximation, the primordial production yield for a particle is given by (49):

$$N^{\text{pri}} = F(m)e^{B\mu_B + S\mu_S + Q\mu_Q}, \quad (8)$$

where  $F(m)$  is a function of the particle mass ( $m$ ).  $B$ ,  $S$ , and  $Q$  are the baryon number, strangeness, and electric charge of the particle, while  $\mu_B$ ,  $\mu_S$ , and  $\mu_Q$  are the chemical potentials of the corresponding conserved quantum numbers. Consequently,

$$N_{\bar{p}}^{\text{pri}} = F(m_p)e^{-\mu_B - \mu_Q}, \quad (9)$$

$$N_d = F(m_d)e^{2\mu_B + \mu_Q}, \quad (10)$$

$$N_{\bar{d}} = F(m_d)e^{-2\mu_B - \mu_Q}, \quad (11)$$

$$N_n^{\text{pri}} = F(m_n \approx m_p)e^{\mu_B} = N_{\bar{p}}^{\text{pri}} \sqrt{N_d/N_{\bar{d}}}. \quad (12)$$

In this equation, the subscripts  $d$  and  $p$  represent deuteron and proton, respectively. Although we derive the equation using the thermal model, the relationship holds in general as long as the deuteron yield is proportional to the yield product of neutrons and protons, as in the coalescence model of nuclei (50, 51). To obtain the primordial antiproton yield, the feed-down fraction to antiproton is evaluated as  $N_{\bar{p}}^{\text{FD}}/N_{\bar{p}}^{\text{inc}} = N_p^{\text{FD}}/N_p^{\text{inc}} \times (N_{\bar{\Lambda}}/N_\Lambda)/(N_{\bar{p}}^{\text{inc}}/N_p^{\text{inc}})$ . To reach this conclusion, we approximate all antihyperon-to-hyperon ratios as  $N_{\bar{\Lambda}}/N_\Lambda$ . The  $N_{\bar{p}}^{\text{inc}}/N_p^{\text{inc}}$  and  $N_{\bar{\Lambda}}/N_\Lambda$  ratios are extracted from Refs. (15, 52).

The antineutron yields are estimated similarly as for neutrons. For the primordial production,  $N_{\bar{n}}^{\text{pri}} = N_p^{\text{pri}} \sqrt{N_{\bar{d}}/N_d}$ . Uncertainties arising from those in feed-down fractions, hyperon ratios, and the possible imbalance of proton and antiproton feed-down fractions are accounted for in the final results.

The estimated neutron and antineutron yields, averaged over Ru+Ru and Zr+Zr collisions and divided by  $\langle N_{\text{part}} \rangle$  (20) to take out trivial geometric effects, are plotted in the right panel of Fig. S3 as a function of centrality. Here, 0-10% denotes the most central collisions while 60-80% represents peripheral collisions. For comparison, yields for protons and antiprotons are also plotted in the left panel.

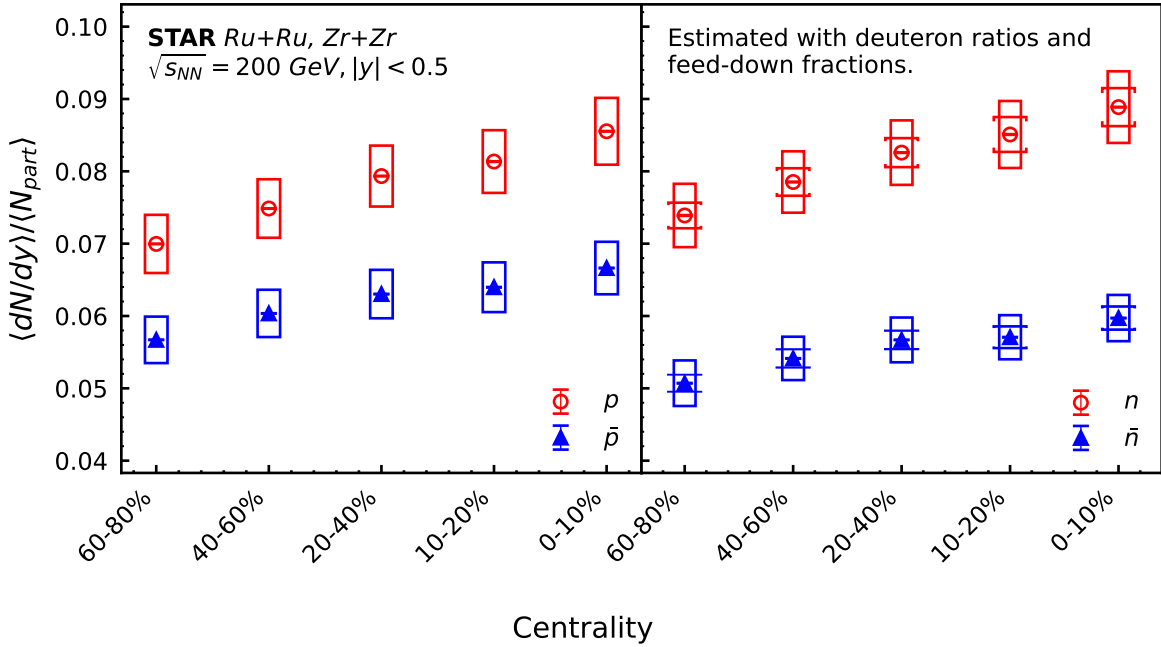


Figure S3: **Proton and neutron yields.** Yields of protons (left) and neutrons (right), as well as their antiparticles, as a function of centrality. Proton and antiproton yields are measured within  $0.45 < p_T < 2.5$  GeV/c and extrapolated to the full  $p_T$  region, while the neutron and antineutron yields are solely estimated. Brackets around data points in the right panel represent uncertainties in the estimation of feed-down contribution, while the boxes in both panels show systematic uncertainties from all other sources.

### 1.1.3 Charge and baryon transport

The net-charge difference between Ru+Ru and Zr+Zr collisions ( $\Delta Q$ ) and the average net-baryon yield ( $\langle B \rangle$ ) among the two collision systems are shown as a function of centrality (20) in the left and right panels of Fig. S4, respectively. Additional uncertainties arising from

unmeasured nuclei in the baryon number calculation, different extrapolation functions used for invariant yields and double ratios, and feed-down related parameters, are also included. Both quantities are scaled with  $\langle N_{\text{part}} \rangle$  and compared to UrQMD calculations (28, 29), which assign valence quarks as the baryon number carriers. For the baryon transport, the UrQMD model employs a Gaussian parameterization for the longitudinal fragmentation to produce more baryons than the Field-Feynman fragmentation (29). Such a parameterization was tuned to match previous experimental data on proton production in heavy-ion collisions by enhancing quark stopping at mid-rapidity, and thus provides a good description of the baryon transport in central Ru+Ru and Zr+Zr collisions (right panel of Fig. S4). However, this tuning results in a factor of 3 larger charge transport difference between Ru+Ru and Zr+Zr collisions from UrQMD than that in data (left panel of Fig. S4).

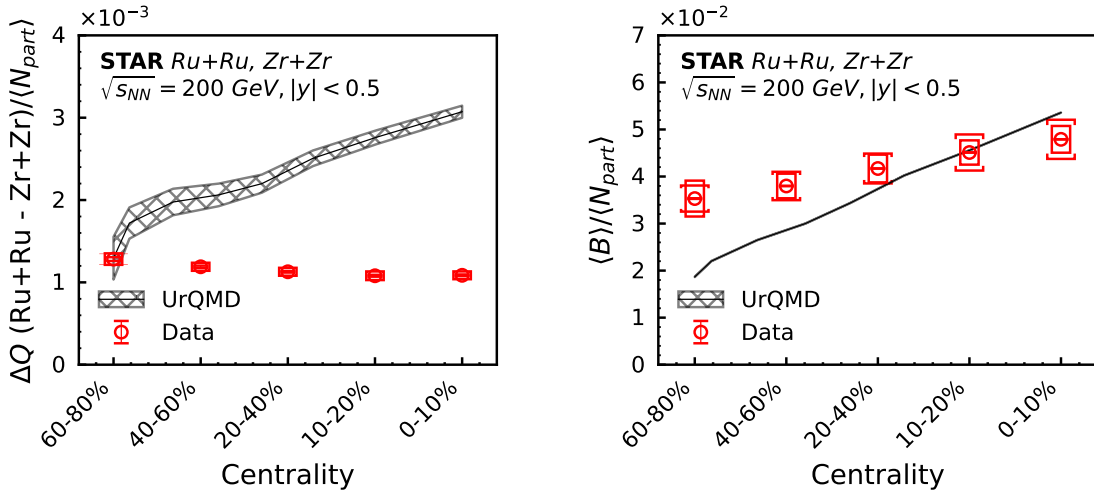


Figure S4: **Comparison between data and UrQMD.** Distributions of net-charge difference (left) and average net-baryon yield (right), scaled by  $\langle N_{\text{part}} \rangle$ , between Ru+Ru and Zr+Zr collisions at  $\sqrt{s_{\text{NN}}} = 200$  GeV as a function of centrality. Red circles represent data with the boxes (vertical bars) around them representing systematic (statistical) uncertainties. Uncertainties due to feed-down correction for net-baryon yields are shown separately as brackets. UrQMD calculations are shown as hatched bands for comparison. In the right panel, the hatched band collapses to a curve due to very small statistical uncertainties.

For the measurement of  $\langle B \rangle / \Delta Q$  ratio, the dominant uncertainties are those associated with feed-down related parameters (6.8-7.2%) and extrapolations of particle yields (2.0-8.3%) and double ratios (3.2-4.6%), where the uncertainty ranges result from their centrality dependence. Other sources of uncertainties typically contribute less than 2%.

## 1.2 Baryon transport in photonuclear events

Studying baryon transport in  $\gamma$ +Au interactions provides another avenue for identifying the baryon number carrier.

The key to selecting  $\gamma$ +Au events is the asymmetric rapidity dependence of produced particles. Model calculations indicate that in such collisions a large amount of activity is expected in the Au-going direction due to nucleus fragmentation, while little-to-no activity is expected in the  $\gamma$ -going direction (*II*). Most importantly, a few neutrons from the fragmenting Au nucleus are expected to be traveling in the Au-going direction, while the  $\gamma$ -going side is expected to see one or two neutrons due to Coulomb excitations. In addition, the rapidity distribution of charged tracks around mid-rapidity is expected to be strongly asymmetric, with more particles in the Au-going direction.

Following those guidelines, to trigger on inclusive  $\gamma$ +Au interactions from Au+Au collisions, we measure the energy distribution of neutrons detected by the Zero Degree Calorimeter detectors (ZDCs). We then identify peaks in the energy distribution that correspond to different numbers of neutrons ( $1n$ ,  $2n$ ,  $\dots$ ,  $Xn$ ). We require the ZDC detector in the  $\gamma$ -going side to have a single neutron hit ( $1n$ ) and more than one neutron ( $Xn$  where  $X > 1$ ) in the Au-going direction. Requiring a single neutron hit ( $1n$ ) instead of zero neutrons ( $0n$ ) in the  $\gamma$ -going direction helps reduce backgrounds from fixed-target and beam-gas events which can also produce rapidity asymmetry of charged particles around mid-rapidity but their fragmenting neutrons would not reach the ZDC. Additional asymmetric cuts on the energy deposition in the Beam-Beam Counter (BBCs) also help to improve the purity of the  $\gamma$ +Au interactions by selecting events with low activity in the  $\gamma$ -going direction and high activity in the Au-going direction. Contamination due to hadronic events can be further reduced by exploiting the timing information from the VPDs. Unlike Au+Au collisions, in  $\gamma$ +Au interactions one of the VPDs sees little activity and so the timing difference between the two VPDs cannot be used to accurately determine the vertex position along the beam direction ( $z$ ). We exploit this characteristic and require significant disagreement between the vertex  $z$  positions measured by the TPC and VPDs:  $\Delta V_z = |V_z^{\text{TPC}} - V_z^{\text{VPD}}| > 10$  cm. For a more detailed description of this trigger, see Ref. (*II*).

With these cuts we select about 2 million  $\gamma$ +Au events from about 100 million minimum bias Au+Au events at  $\sqrt{s_{\text{NN}}} = 54.4$  GeV. Due to the selection criteria used, this data sample is biased toward high multiplicity  $\gamma$ +Au interactions, where the average number of charged tracks within  $|y| < 0.5$  is about 7.

The proton and antiproton yields are extracted by using the  $m^2$  distribution of charged tracks measured by TOF, and requiring  $0.7 < m^2 < 1.06$  GeV<sup>2</sup>/c<sup>4</sup>. They are corrected for the  $m^2$  cut efficiency, evaluated by fitting the  $m^2$  distribution with a Student's t-function. As aforementioned, VPDs supply collision start time for the  $m^2$  calculation, and the VPD signal from only the Au-going side can still provide sufficient timing resolution for an accurate start time determination. The presented results focus on total yields of protons and antiprotons, and therefore contributions from weak decays are not subtracted.

Measured proton and antiproton yields are corrected for various contaminations. The first correction is related to the contamination from peripheral Au+Au events, dominantly those in the 80-100% centrality class. The fraction ( $r$ ) of peripheral events in the selected  $\gamma$ +Au sample is estimated to be about 11-13% depending on which colliding Au nucleus is chosen as the photon emitter. Due to the complications in correcting for the trigger bias, it is difficult to measure particle yields in collisions that are more peripheral than 80%, so protons and antiprotons from 60-80% peripheral collisions are used as an estimate of the peripheral background ( $Y_p^{AA}$ ). A multiplicative factor ( $f$ ) is used to account for the multiplicity difference between 60-80% and 80-100% events. The corrected yield for  $\gamma$ +Au processes ( $Y_p^{\gamma A}$ ) is as follows:

$$Y_p^{\gamma A} = \frac{Y_p^{\gamma A+AA} - r f Y_p^{AA}}{1 - r}, \quad (13)$$

where  $Y_p^{\gamma A+AA}$  denotes the proton or antiproton yield in the selected  $\gamma$ +Au events.

Corrections for the TPC tracking efficiency and energy loss, TOF matching efficiency and knock-out proton contamination are evaluated similarly as outlined in Sec. 1.1. The proton and antiproton spectra for  $\gamma$ +Au collisions, shown in Fig. S5, are the average spectra for the cases when the photon is emitted by either of the two colliding Au nuclei. We define the proton rapidity under the condition that the photon always travels in the negative  $y$  direction. The solid curves represent Lévy function fits used to extract the rapidity density ( $dN/dy$ ). The Lévy function is a generalized exponential function:  $A(1 + \frac{m_T - m_p}{Cn})^{-n}$ , where  $m_p$  is the proton mass,  $m_T = \sqrt{p_T^2 + m_p^2}$  is the transverse mass,  $A$  is a normalization factor,  $C$  is a characteristic transverse mass scale, and  $n$  is a shape parameter that controls the slope of the spectra at high  $m_T$ .

The total relative systematic uncertainties of the  $dN/dy$  values are on average about 13% for protons and about 8% for antiprotons. It is dominated by the uncertainties due to the  $\gamma$ +Au event selection. We find the difference in the  $dN/dy$  values between events where either Au nucleus in Au+Au collisions emits the photon (4% for protons and negligible for antiprotons). We also change the selection on the VPD, requiring no activity on the  $\gamma$ -going side instead of the default cut of requiring significant disagreement between the vertex  $z$  positions as measured by the TPC and VPD detectors (8% for protons and 3% for antiprotons). The uncertainty due to extrapolation is estimated by comparing the  $dN/dy$  values extracted with a Blast-wave function to the default results and contributes about 5% for protons and 2% for antiprotons. Various other sources of systematic uncertainties are also considered. These sources include tracking efficiency uncertainty (5%), contribution of beam gas and beam pipe events (3%), track selection uncertainty (1%) (using different criteria), peripheral event contamination (4%), knock-out proton correction uncertainty (<1% for protons), uncertainty in track background from  $m^2$  fits (< 0.1%), uncertainty related to particle identification (2% for protons and 5% for antiprotons), the uncertainty of the efficiency correction for the  $m^2$  cut (<1%) and missing weak decays (0.6%).

When fitting the net-proton  $dN/dy$  distribution to extract the slope parameter, we separate

the systematic uncertainties into those which affect the  $dN/dy$  distribution with a clear  $y$  dependence (“correlated”) and those that do not (“uncorrelated”). For correlated sources, we fit shifted  $dN/dy$  values separately, and the uncertainty is set to be the difference between the shifted slope and the default one divided by  $\sqrt{3}$ . The uncorrelated uncertainties are added in quadrature with the statistical uncertainties to obtain the total uncorrelated uncertainties, which are then used for the  $dN/dy$  fitting.

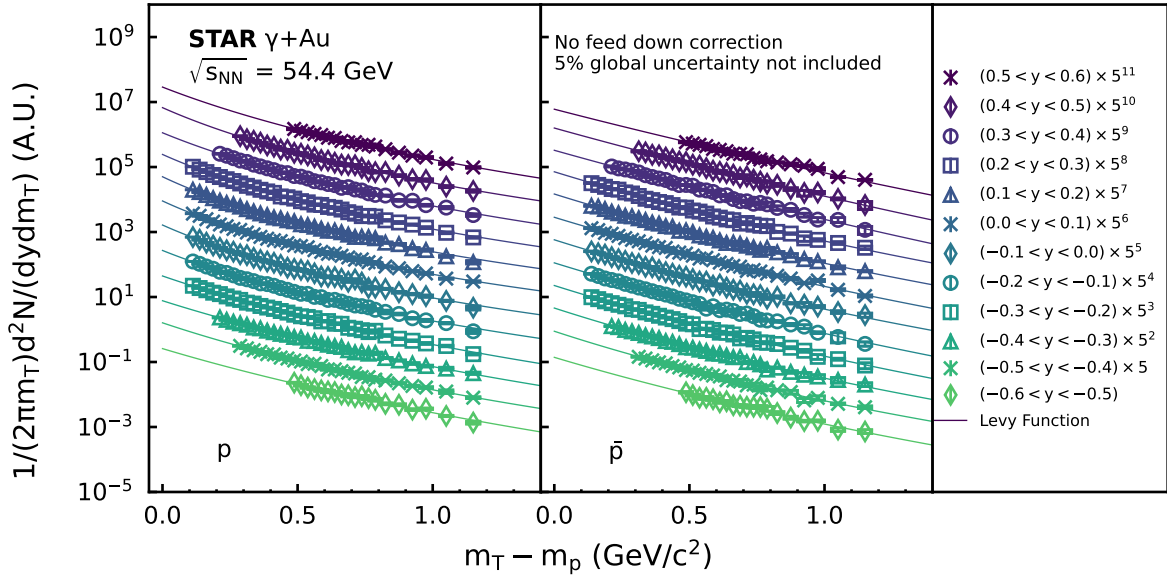


Figure S5: **(Anti)proton spectra in  $\gamma$ +Au.** The proton and antiproton  $m_T$  spectra in  $\gamma$ +Au processes selected from Au+Au collisions at  $\sqrt{s_{\text{NN}}} = 54.4$  GeV. Solid curves represent fits to the spectra with the Lévy function.

## References

1. Sakharov, A. D. Violation of CP Invariance, C asymmetry, and baryon asymmetry of the universe. *Pisma Zh. Eksp. Teor. Fiz.* **5**, 32–35 (1967).
2. Sarkar, U. *Particle and astroparticle physics*. Series in high energy physics, cosmology, and gravitation (Taylor & Francis, New York, USA, 2008).
3. Artru, X. String model with baryons: Topology; classical motion. *Nucl. Phys. B* **85**, 442–460 (1975).
4. Rossi, G. C. & Veneziano, G. A possible description of baryon dynamics in dual and gauge theories. *Nucl. Phys. B* **123**, 507–545 (1977).

5. Kharzeev, D. Can gluons trace baryon number? *Phys. Lett. B* **378**, 238–246 (1996). [nucl-th/9602027](#).
6. Suganuma, H., Takahashi, T. T., Okiharu, F. & Ichie, H. Lattice QCD study for the interquark force in three-quark and multi-quark systems. *AIP Conf. Proc.* **756**, 123–132 (2005). [hep-lat/0412026](#).
7. Takahashi, T. T., Matsufuru, H., Nemoto, Y. & Suganuma, H. Three-quark potential in the SU(3) lattice QCD. *Phys. Rev. Lett.* **86**, 18–21 (2001). [hep-lat/0006005](#).
8. Bissey, F. *et al.* Gluon flux-tube distribution and linear confinement in baryons. *Phys. Rev. D* **76**, 114512 (2007).
9. Csorgo, T., Gyulassy, M. & Kharzeev, D. Buckyballs and gluon junction networks on the femtometer scale. *J. Phys. G* **30**, L17–L25 (2004). [hep-ph/0112066](#).
10. Rossi, G. & Veneziano, G. The string-junction picture of multiquark states: an update. *JHEP* **06**, 041 (2016). [1603.05830](#).
11. Lewis, N. *et al.* Search for baryon junctions in photonuclear processes and isobar collisions at RHIC. *Eur. Phys. J. C* **84**, 590 (2024). [2205.05685](#).
12. Gyulassy, M., Topor Pop, V. & Vance, S. E. Baryon number transport in high-energy nuclear collisions. *Acta Phys. Hung. A* **5**, 299–318 (1997). [nucl-th/9706048](#).
13. Appelshauser, H. *et al.* Baryon stopping and charged particle distributions in central Pb+Pb collisions at 158 GeV per nucleon. *Phys. Rev. Lett.* **82**, 2471–2475 (1999). [nucl-ex/9810014](#).
14. Arsene, I. C. *et al.* Nuclear stopping and rapidity loss in Au+Au collisions at  $\sqrt{s_{NN}} = 62.4$  GeV. *Phys. Lett. B* **677**, 267–271 (2009). [0901.0872](#).
15. Abelev, B. I. *et al.* Systematic measurements of identified particle spectra in *pp*, *d*+Au and Au+Au collisions at the STAR detector. *Phys. Rev. C* **79**, 034909 (2009). [0808.2041](#).
16. Christiansen, J. R. & Skands, P. Z. String formation beyond leading colour. *JHEP* **08**, 003 (2015). [1505.01681](#).
17. Bierlich, C. *et al.* A comprehensive guide to the physics and usage of PYTHIA 8.3. *SciPost Phys. Codebases* **8** (2022). [2203.11601](#).
18. Lönnblad, L. & Shah, H. Baryon correlations in Pythia. *Eur. Phys. J. C* **83**, 1105 (2023). [2309.01557](#).
19. Bellm, J. *et al.* Herwig 7.0/Herwig++ 3.0 release note. *Eur. Phys. J. C* **76**, 196 (2016). [1512.01178](#).

20. Abdallah, M. *et al.* Search for the chiral magnetic effect with isobar collisions at  $\sqrt{s_{\text{NN}}} = 200$  GeV by the STAR Collaboration at the BNL Relativistic Heavy Ion Collider. *Phys. Rev. C* **105**, 014901 (2022). 2109.00131.
21. Artru, X. & Mekhfi, M. What can we learn from unpolarized and polarized electroproduction of fast baryons? *Nucl. Phys. A* **532**, 351–357 (1991).
22. Adamczyk, L. *et al.* Bulk properties of the medium produced in relativistic heavy-ion collisions from the beam energy scan program. *Phys. Rev. C* **96**, 044904 (2017). 1701.07065.
23. Materials and methods are available as supplementary materials .
24. Whalley, M. R. A compilation of data on hadronic total cross-sections in  $e^+e^-$  interactions. *J. Phys. G* **29**, A1–A133 (2003).
25. Riordan, E. M. The discovery of quarks. *Science* **256**, 1287–1293 (1992).
26. Ackermann, K. H. *et al.* STAR detector overview. *Nucl. Instrum. Meth.* **A499**, 624–632 (2003).
27. Schnedermann, E., Sollfrank, J. & Heinz, U. W. Thermal phenomenology of hadrons from 200A GeV S+S collisions. *Phys. Rev. C* **48**, 2462–2475 (1993). nucl-th/9307020.
28. Bass, S. A. *et al.* Microscopic models for ultrarelativistic heavy ion collisions. *Prog. Part. Nucl. Phys.* **41**, 255–369 (1998). nucl-th/9803035.
29. Bleicher, M. *et al.* Relativistic hadron-hadron collisions in the ultra-relativistic quantum molecular dynamics model. *J. Phys. G* **25**, 1859–1896 (1999). hep-ph/9909407.
30. Xu, H.-j. *et al.* Measuring neutron skin by grazing isobaric collisions. *Phys. Rev. C* **105**, L011901 (2022). 2105.04052.
31. Lin, Z.-W., Ko, C. M., Li, B.-A., Zhang, B. & Pal, S. A Multi-phase transport model for relativistic heavy ion collisions. *Phys. Rev. C* **72**, 064901 (2005). nucl-th/0411110.
32. von Weizsacker, C. F. Radiation emitted in collisions of very fast electrons. *Z. Phys.* **88**, 612–625 (1934).
33. Williams, E. J. Nature of the high energy particles of penetrating radiation and status of ionization and radiation formulae. *Phys. Rev.* **45**, 729–730 (1934).
34. Wang, X. *et al.* Collision-energy dependence of the Breit-Wheeler process in heavy-ion collisions and its application to nuclear charge radius measurements. *Phys. Rev. C* **107**, 044906 (2023). 2207.05595.

35. Itakura, K., Kovchegov, Y. V., McLerran, L. & Teaney, D. Baryon stopping and valence quark distribution at small  $x$ . *Nucl. Phys. A* **730**, 160–190 (2004). [hep-ph/0305332](#).
36. Accardi, A. *et al.* Electron-Ion Collider: The next QCD frontier. *Eur. Phys. J. A* **52**, 268 (2016). [1212.1701](#).
37. Cebra, D., Sweger, Z., Dong, X., Ji, Y. & Klein, S. R. Backward-angle (u-channel) production at an electron-ion collider. *Phys. Rev. C* **106**, 015204 (2022). [2204.07915](#).
38. Anderson, M. *et al.* The STAR time projection chamber: a unique tool for studying high multiplicity events at RHIC. *Nucl. Instrum. Meth.* **A499**, 659–678 (2003). [nucl-ex/0301015](#).
39. Llope, W. J. *et al.* The TOFP / pVPD time-of-flight system for STAR. *Nucl. Instrum. Meth. A* **522**, 252–273 (2004). [nucl-ex/0308022](#).
40. Bichsel, H. A method to improve tracking and particle identification in TPCs and silicon detectors. *Nucl. Instrum. Meth.* **A562**, 154–197 (2006).
41. Llope, W. J. *et al.* The STAR Vertex Position Detector. *Nucl. Instrum. Meth.* **A759**, 23–28 (2014). [1403.6855](#).
42. Brun, R., Bruyant, F., Maire, M., McPherson, A. C. & Zanarini, P. GEANT3. *CERN-DD-EE-84-01* (1987).
43. Adam, J. *et al.* Beam energy dependence of (anti-)deuteron production in Au+Au collisions at the BNL Relativistic Heavy Ion Collider. *Phys. Rev. C* **99**, 064905 (2019). [1903.11778](#).
44. Adler, C. *et al.* Anti-deuteron and anti- $^3\text{He}$  production in  $\sqrt{s_{\text{NN}}} = 130$  GeV Au+Au collisions. *Phys. Rev. Lett.* **87**, 262301 (2001). [Erratum: *Phys. Rev. Lett.* **87**, 279902 (2001)], [nucl-ex/0108022](#).
45. Workman, R. L. *et al.* Review of Particle Physics. *Prog. Theor. Exp. Phys.* **2022**, 083C01 (2022).
46. Adams, J. *et al.* Strange antiparticle-to-particle ratios at mid-rapidity in  $\sqrt{s_{\text{NN}}} = 130$  GeV Au+Au collisions. *Phys. Lett. B* **567**, 167–174 (2003). [nucl-ex/0211024](#).
47. Abelev, B. I. *et al.* Identified baryon and meson distributions at large transverse momenta from Au+Au collisions at  $\sqrt{s_{\text{NN}}} = 200$  GeV. *Phys. Rev. Lett.* **97**, 152301 (2006). [nucl-ex/0606003](#).
48. Wheaton, S. & Cleymans, J. THERMUS: A Thermal model package for ROOT. *Comput. Phys. Commun.* **180**, 84–106 (2009). [hep-ph/0407174](#).

49. Senger, P. Particle production in heavy-ion collisions. *Prog. Part. Nucl. Phys.* **53**, 1–23 (2004).
50. Schwarzschild, A. & Zupancic, C. Production of tritons, deuterons, nucleons, and mesons by 30-GeV protons on A-1, Be, and Fe targets. *Phys. Rev.* **129**, 854–862 (1963).
51. Gutbrod, H. H. *et al.* Final state interactions in the production of hydrogen and helium isotopes by relativistic heavy ions on uranium. *Phys. Rev. Lett.* **37**, 667–670 (1976).
52. Adams, J. *et al.* Scaling properties of hyperon production in Au+Au collisions at  $\sqrt{s_{NN}} = 200$  GeV. *Phys. Rev. Lett.* **98**, 062301 (2007). nucl-ex/0606014.